Earth and Planetary Science Letters 553 (2021) 116615

Contents lists available at ScienceDirect

Earth and Planetary Science Letters

www.elsevier.com/locate/epsl

Warm and oxidizing slabs limit ingassing efficiency of nitrogen to the mantle

Colin R.M. Jackson [a,*], Elizabeth Cottrell [b], Ben Andrews [b]

[a] Department of Earth and Environmental Sciences, Tulane University, USA
[b] Department of Mineral Sciences, National Museum of Natural History, Smithsonian Institution, USA

ARTICLE INFO

Article history:
Received 30 May 2020
Received in revised form 10 September 2020
Accepted 26 September 2020
Available online 12 October 2020
Editor: R. Dasgupta

Keywords:
nitrogen
slab
partitioning

ABSTRACT

Nitrogen is a major and essential component of Earth's atmosphere, yet relative to other volatile elements, there are relatively few experimental constraints on the pathways by which nitrogen cycles between Earth's interior and exterior. We report mineral-melt and mineral-fluid partitioning experiments to constrain the behavior of nitrogen during slab dehydration and sediment melting processes. Experiments reacted rhyolitic melts with silicate and oxide minerals, in the presence of excess aqueous fluid, over temperatures between 725-925 °C and pressures between 0.2 and 2.3 GPa. Oxygen fugacity ranged between iron metal saturation (∼NNO-5) to that in excess of primitive arc basalts (∼NNO+2). Our experiments demonstrate that hydrous fluid is the preferred phase for nitrogen over minerals (biotite, K-feldspar, and amphibole) and rhyolitic melts across all conditions explored. Relatively large effects of pressure ($\log(D^{N}_{melt-fluid})/$ (GPa/K) = 761 ± 68 (1σ), $\log(D^{N}_{biotite-fluid})/$ (GPa/K) = 462 ± 169) and moderate effects of oxygen fugacity ($log(D^{N}_{melt-fluid})/$ NNO = -0.20 ± 0.04, $\log(D^{N}_{biotite-fluid})/$ NNO = -0.10 ± 0.04) modulate partitioning of nitrogen. We further document negligible partitioning effects related to mineral composition or Cl content of hydrous fluid. Of the minerals investigated, biotite has the largest affinity for N and should control the retention of N in slabs where present. Application of partitioning data to slab dehydration PT paths highlights the potential for highly incompatible behavior ($D^{N}_{biotite-fluid}$ < 0.1) from the slab along warmer and oxidized (NNO+1) subduction geotherms, whereas dehydration along reduced and cooler geotherms will extract moderate amounts of nitrogen ($D^{N}_{biotite-fluid}$ > 0.1). We find that slab melting is less effective at extracting N from slabs than fluid loss, at least under oxidized conditions (NNO+1). Ultimately, the conditions under which slabs lose fluid strongly affect the distribution of nitrogen between Earth's interior and exterior.

1. Introduction

Reactive, highly volatile elements (e.g. H, C, N) are essential for life and impact climate. Among these elements, N is unique in its strong partitioning into near-surface reservoirs (Fig. 1a, Marty, 2012), defined here as the sum of N contained in the crust, oceans, and atmosphere relative to the mantle that sources mid-ocean ridge basalts (MORB). Indeed, accumulation of N into near-surface reservoirs relative to MORB mantle is ∼10× and ∼5× greater than C and H (Marty, 2012; Halliday, 2013), respectively. Sufficient N is input into subduction zones, primarily residing in slab sediments (e.g., Halama et al., 2014), such that, without a return flux, the entire atmosphere would be drawn into the mantle at current plate rates over 4.5 Gyrs (Johnson and Goldblatt, 2015). Current observations suggest, however, that the partial pressure of nitrogen in the atmosphere (p_{N2}) may have actually increased from ∼3 Ga to the modern (Marty et al., 2013; Som et al., 2016). A thickening, or even slowly thinning, atmosphere is consistent with inefficient return of N to the deep Earth. Efficient subduction should lead to geologically rapid drawdown of atmospheric N.

Inefficient return of N to the deep Earth likely reflects the stability of N_2, and potentially other neutral species, at or near Earth's surface. Nitrogen, when speciated as N_2, behaves as a noble gas similar to Ar (e.g., Libourel et al., 2003), hindering the regassing of atmospheric N into the mantle via subduction. An important observation, however, is that the partitioning of Ar (non-radiogenic) into near-surface reservoirs is nearly 50× greater than that observed for N (Fig. 1a). Thus, N occupies a chemical middle-ground

* Corresponding author.
E-mail address: cjackson2@tulane.edu (C.R.M. Jackson).

https://doi.org/10.1016/j.epsl.2020.116615
0012-821X/

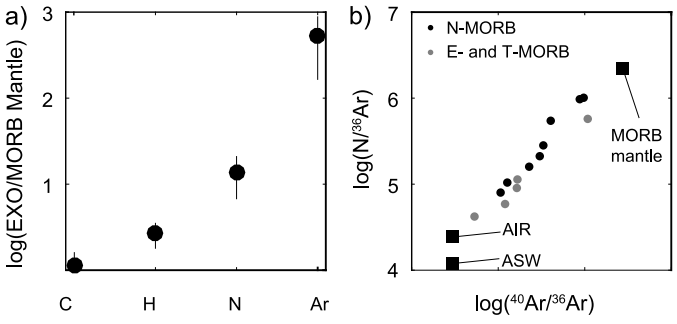

Fig. 1. Global constraints on the deep cycling of N. (a) Distribution of various highly volatile elements between near-surface reservoirs (atmosphere, crust, oceans) and MORB mantle. Volatiles that are stoichimetric constituents of subducted minerals show relatively weak partitioning into near-surface reservoirs compared to unreactive gases, such as Ar. Nitrogen occupies a position intermediate to these two classes of volatiles. Data are from Marty (2012). (b) The Ar-N systematics of gases extracted from MORB are well explained by mixing between a mantle reservoir with nearly constant N/^{40}Ar and the near surface reservoirs of the atmosphere and air-saturated seawater (ASW). The homogeneity of N/^{40}Ar in MORB mantle suggests consistent coupling of N and K during their respective deep cycles. Data are from Marty and Zimmermann (1999).

between the more reactive volatile elements, C and H, and the more inert noble gases. The exact position of N within this range of geochemical behavior likely reflects the competing influences of neutral and other, more chemically reactive, species of N (Fig. 1a).

A clue regarding the identity of the reactive N species comes from the strong correlation between N and ^{40}Ar in rocks derived from MORB mantle (Fig. 1b) (Marty, 1995; Johnson and Goldblatt, 2015). ^{40}Ar is exclusively produced by the decay of K, and the correlation between N and ^{40}Ar is consequently explained by the long-term coupling of N and K in mantle environments. We note that there is a mantle component, most commonly and strongly expressed in ocean island basalts (OIB), with very high N/^{40}Ar ratios (>10,000) compared to the MORB mantle (124±40) (Marty and Zimmermann, 1999; Johnson and Goldblatt, 2015). Here we focus on the relatively well-established distribution of N between Earth's near surface reservoirs and MORB mantle.

The distribution of K in MORB mantle is affected by recycling of surficial materials back into the mantle, and thus, the coupling of N and K in MORB mantle suggests these two elements are recycled together. Nitrogen, when speciated as the ammonium ion (NH_4^+), is expected to couple with K (Marty and Dauphas, 2003). NH_4^+ is monovalent and large radius, like K. Indeed, laboratory experiments have confirmed complete solid solution between K- and NH_4-endmember feldspar and muscovite (Pöter et al., 2004).

Additional evidence for the link between NH_4^+ and K-bearing minerals comes from rocks exhumed from subduction zones. Bulk rock K_2O and N are correlated within a wide range of metamorphic terranes (Bebout and Fogel, 1992; Busigny et al., 2003; Halama et al., 2016). Metasedimentary rocks can contain N concentrations upwards of 1000 ppm, with the large majority identified as NH_4^+ within mica (Bebout and Fogel, 1992; Sadofsky and Bebout, 2000; Busigny et al., 2003; Plessen et al., 2010; Johnson and Goldblatt, 2015). MORB mantle N contents are estimated to be ~0.25 ppm (Marty and Dauphas, 2003), for comparison. In addition, N contents of exhumed rocks decrease with increasing metamorphic grade, and fractional loss of N is typically larger than loss of K (Bebout and Fogel, 1992; Palya et al., 2011; Plessen et al., 2010). If N were perfectly coupled to K during prograde metamorphism, then the loss of N and K should be matched. Thus, the preferential loss of N compared to K suggests NH_4^+ is not the only species controlling the behavior of N during subduction. Mixed N species stability is also implied by N isotopic variations within prograde metamophric rocks (Bebout and Fogel, 1992; Mingram and Bräuer, 2001). The likelihood that N exists as mixed species in subduction environments aligns with the degree of N partitioning into near-surface reservoirs, where it occupies the middle-ground between volatile elements that are stoichiometric components of common minerals (C and H) in the slab and noble gases (Fig. 1a).

If N is a mixed species element within subduction environments, then its geochemical behavior will be strongly dependent on the thermodynamic parameters present within slabs. Reaction (1) describes the stability of NH_4^+ relative to N_2:

$$2N_2 + 6H_2O + 4H^+ = 4NH_4^+ + 3O_2 \quad (1)$$

And the relative stabilities of NH_4^+, NH_3, and NH_2^- (amide anion) follow Reactions (2) and (3):

$$NH_3 + H^+ = NH_4^+ \quad (2)$$

$$NH_3 = NH_2^- + H^+ \quad (3)$$

The stability of NH_4^+ relative to other species (e.g., N_2, NH_3, NH_2^-) depends on pressure (P) and temperature (T), as well as bulk composition, oxygen fugacity (fO_2) and pH (we refer to these combined compositional parameters as X), following Reactions (1)-(3) (Mikhail and Sverjensky, 2014; Li and Keppler, 2014; Chen et al., 2019; Mikhail et al., 2017; Mallik et al., 2018). Each species will also have its own, unique partitioning behavior between minerals, melts, and fluids that also depends on *P-T-X* conditions. Partitioning is defined here as the wt.% ratio of nitrogen in either minerals or melts over fluid (e.g., $D^N_{mineral-fluid}$ = mineral wt.% N / fluid wt.% N), when the concentrations reflect an equilibrium distribution. Nitrogen that is partitioned into minerals is retained in the slab, while nitrogen partitioned into fluid and melt can be lost to the mantle wedge and ultimately returned to the atmosphere. A portion of the N fluxed into the mantle wedge may be retained in secondary serpentinites (e.g., Cannaò et al., 2020).

Neutral species, akin to Ar, are expected to partition into fluids over melts and minerals despite some capacity of slab minerals to incorporate these species (~1-100 ppb/bar of neutral species fugacity; Jackson et al., 2015; Krantz et al., 2019), while experiments show that NH_4^+ partitions nearly evenly between muscovite, K-feldpsar and fluid (Pöter et al., 2004). Thus, the capacity of a slab to retain N during mass loss is likely a complex function of both the stability of NH_4^+ (Reactions (1)-(3)) and the partitioning of NH_4^+ between K-bearing minerals, melt, and fluid.

Using this framework, we seek to experimentally quantify how efficiently N is lost from slabs undergoing dehydration and melting by measuring the reactivity of N with silicate, both minerals and melts. The majority of N in slabs is initially reduced by biologic activity within the oceans and is therefore concentrated within sediments and, to a lesser degree, the underlying uppermost oceanic crust (Li et al., 2007; Halama et al., 2014; Busigny et al., 2019). Available evidence suggests the reactivity of N with rock is controlled by the exchange of NH_4^+ into minerals with stoichiometric K. Micas are major K-bearing phases for metasediments and metabasalt, with muscovite being present at lower P/T conditions, biotite having a wide stability field up to 2.5 GPa and temperatures associated with slab melting, and phengite being stable beyond 2.5 GPa (e.g., Johnson and Plank, 2000; Schmidt et al., 2004). Feldspars and amphibole can also have stoichiometric K and are stable under certain slab *P-T-X* conditions (e.g., Johnson and Plank, 2000). Our experiments were consequently designed to produce relatively large grains of mica (biotite), feldspar (Na- and K-rich), and amphibole (hornblende) in equilibrium with hydrous fluid and rhyolitic melt to study the behavior of N during dehydration and melting processes up to 2.3 GPa and 925 °C. Our work quantifying N reactivity with minerals builds from previous efforts where nitrogen behavior in slab systems was inferred from N speciation in fluids and melt-fluid partitioning (e.g., Li and Keppler, 2014; Li et al., 2015; Mallik et al., 2018).

2. Methods

We conducted two series of experiments. A piston cylinder (PC) apparatus was used in the first series to determine the *P, T*, fO_2, and Cl effects on N partitioning. PC experimental conditions were 0.95-2.3 GPa and 775-925 °C, with durations of 1-95 hours. Externally-heated cold-seal pressure vessels (cold seals, CS) were used in the second series to corroborate the fO_2 effect, anchor the lower end of the pressure series, and to stabilize feldspar. CS experimental conditions were 0.15-0.2 GPa and 725-775 °C, with durations of 24-105 hours. Waspaloy (Ni-rich) alloy was used for all CS experiments. Table 1 details run conditions. Details of the methods, including preparation of the starting materials, run procedures, and analysis are given in the supplementary text.

2.1. Starting material preparation

The blend of starting materials each experiment is reported in Table 1, and the major element compositions of the starting silicates are reported in Supplementary Table 1. Briefly summarized here, CS series experiments used a mixture of glasses with biotite, K-feldspar, rhyolite compositions as the starting silicate materials, with the exception of CS_NK_60. PC series experiments utilized a starting hydroxide mixture (HY3) as the starting silicate, with the exception of PC_NK_3 and 4, which used mixtures of glasses, following approach of the majority of the CS series. CS_NK_EXP60 used a hydroxide mixture, following the approach of the PC series. All experiments that used mixtures of glasses as the starting silicate had N introduced as a N-bearing fluid. Fluids are labeled either "1:1" or "3:1" in Table 1. Ratios denote the weight fraction of N-bearing to K-bearing components in the fluid. All experiments that used hydroxide starting materials had N introduced as NH_4Cl, NH_4NO_3, or a mixture of NH_4Cl and NO_3NH_4. Hydroxides decompose to produce water at experimental temperatures. The supplementary text provides additional details regarding starting materials.

2.2. Capsule preparation

We modulated fO_2 and fluid chemistry using a double capsule approach. A welded outer Au capsule contained a hydrous fluid, a solid fO_2 buffer, and a Pt sample capsule. We chose Au to limit hydrogen loss to the surroundings during the experiment. We chose Pt to maximize hydrogen exchange between the outer and sample capsules. We presaturated Pt capsules with Fe only in CS experiment numbers, 33-39, and 54. The presaturation step was eliminated because retaining a specific concentration of FeO in the quenched melt was not deemed necessary. PC series experiments with presaturated capsules also cracked during compression due to their relatively high Fe contents, rendering the Pt alloy brittle during compression. Experiments that were run with pure Pt sample capsules had ∼1 mg of Fe added to counteract the effects of Fe loss on the silicate composition.

Table 1 reports the run conditions, fO_2 buffer for each experiment, the composition of fluid added to the outer capsule, and whether a Fe-saturated or unsaturated capsule was used. CS experiments contained ∼100 mg of redox buffer in the outer capsule, ∼30 mg of N-bearing hydrous fluid in contact with the buffer, ∼40 mg starting silicate, and ∼20 mg fluid in contact with the silicate. PC experiments contain ∼50 mg of redox buffer, ∼15 mg of fluid in contact with the buffer, and ∼15 mg of sample mass. Sample mass includes fluid and silicate for PC series experiments.

Several experiments that were run with Fe-oxide buffers used a modified double capsule approach in an attempt to more directly impose a given redox state. In these experiments, we simply crimped the inner capsule. This allowed for direct exchange of fluid between the outer and inner capsules. Experiments run using this capsule design are also noted in Table 1.

2.3. Electron microprobe

Nitrogen concentrations were quantified using a LDE5L diffracting crystal (JEOL 8530F, Smithsonian Institution). This crystal is ∼15× more sensitive to N than the LDE1L crystal, which is typically used for N analysis in JEOL electron microprobes. The added precision that the LDE5L provides is crucial to quantifying the low N concentrations of the experiments reported here. The major drawback to N analysis using the LDE5L is that there is a significant "ghost peak" in the background local to the N Ka peak (Supplementary Figure 1, Supplementary Table 2). Accurate analysis of low N concentrations therefore requires an additional blank correction, but the residual intensity of the ghost peak varies between materials. To address this significant issue, N-free minerals and quenched melt were synthesized using the same methods outlined above for N-bearing experiments. These phases were analyzed repeatedly to yield average ghost peak intensity values that were then subtracted from the corresponding analyses of N-bearing phases. Supplemental Table 2 reports the ghost peak count rate associated with each phase analyzed using the LDE5L crystal. Table 1 reports the N concentrations determined in experiments using the LDE5L crystal, and Supplementary Table 3 reports the count rates for the LDE5L analyses.

We calculate the N sensitivity of the LDE5L crystal by correlating its count rate with simultaneous LDE1L analyses of N over a range of silicate glasses with high N concentrations (Supplementary Figure 2a). This correlation yields a working curve for N analysis by LDE5L on materials with broadly similar matrices to the unknowns. The sensitivity of the LDE5L crystal using the approach is N wt.% = 0.105 ± 0.039 cps/nA (1σ). The accuracy of LDE1L measurements of calibration glasses is verified by the measurement of an external hyalophane standard (900 ± 300 ppm measured versus 1200 ppm nominal, Beran et al., 1992). The 1:1 correlation between LDE1L and LDE5L concentration measurements of experiments is plotted in Supplementary Figure 2b. Additional details on electron microprobe analysis are available in the Supplementary Information.

2.4. Raman spectroscopy

We report Raman spectra collected from the quenched melt for a subset of our experiments that anchor the various N partitioning trends we observe (below) along with fluids containing NH_4NO_3 and NH_4Cl (Supplementary Figures 3 and 4). Data were collected with a Horiba LabRAM HR Evolution microscope (Smithsonian). Spectra were collected using a 405 nm laser and a power of a 4.3 mW at the focal spot on the sample (∼ 1 μm). Test spectra with lower power produced similar spectra. Light was collected through a 100× objective lens and passed through a secondary confocal aperture. A grating with 600 or 300 grooves per mm was used to diffract the light. Spectra were recorded from Raman shits of 400–4500 cm^{-1} with a total integration time of 600 s. Spectra are reported in Supplementary Table 4.

2.5. XANES

We collected Fe K-edge XANES spectra on quenched melts from experiments and standard glasses at station 13-ID-E, Advanced Photon Source (Supplementary Figure 5, Supplementary Table 5), using methods from Cottrell et al. (2018) in order to estimate the experimental fO_2 from the oxidation state of Fe in the quenched silicate melt. Pre-edge peak intensities are low in the hydrous, high-silica quenched melt equilibrated in the cold-seal apparatus

Table 1
Experimental run Conditions and N concentrations.

	series	T (°C)	P (GPa)	dur (h)	capsule	Fluid components	start comp.	silicate (g)	inner cap. fluid (g)	buffer	NNO	N fl. (wt%)	Cl fl. (wt%)	N melt (wt%)	±, 1σ	N K-spar (wt%)	±, 1σ	N biotite (wt%)	±, 1σ	phases present	Note
CS-NK-EXP33	CS time	775	0.15	66	saturated	1:1 NH_4Cl, KCl fl.	C	0.039	0.017	NNO	0.00	2.44	12.20	0.020	0.011					M, Bio, K-spar, Na-spar, Cor	
CS-NK-EXP34	CS time	725	0.20	48	saturated	3:1 NH_4Cl, KCl fl.	C	0.027	0.014	NNO	0.00	6.41	18.82	0.108	0.015	0.024	0.014			M, Bio, K-spar, Na-spar, Cor, Qtz	
CS-NK-EXP37	CS time, CS $fO2$	740	0.20	105	saturated	3:1 NH_4Cl, KCl fl.	C	0.037	0.020	NNO	0.00	6.41	18.82	0.010	0.009			0.045	0.026	M, Bio, K-spar, Na-spar, Cor, Qtz	
CS-NK-EXP39	CS$fO2$	750	0.20	102	saturated	3:1 NH_4Cl, KCl fl.	C2	0.038	0.019	CCO	-1.43	6.41	18.82	0.111	0.008	0.034	0.010	0.194	0.073	M, Bio, K-spar, Na-spar, Cor, Qtz	
CS-NK-EXP51	CS time, CS $fO2$	775	0.20	90	unsaturated	3:1 NH_4Cl, KCl fl.	CS20GL	0.057	0.018	NNO	0.00	6.41	18.82	0.014	0.008					M, Sp, Qtz, Cor, Qtz	
CS-NK-EXP53	CS $fO2$	775	0.20	98	unsaturated	3:1 NH_4Cl, KCl fl.	CS20GL	0.054	0.018	CCO	-1.43	6.41	18.82	0.065	0.009					M, Sp, Qtz, Cor, Qtz	
CS-NK-EXP54	CS time, CS $fO2$	775	0.20	98	saturated	3:1 NH_4Cl, KCl fl.	CS20GL	0.038	0.010	NNO	0.00	6.41	18.82	0.034	0.009					M, Sp, Qtz, Cor, Qtz	
CS-NK-EXP55	CS time, CS $fO2$	775	0.20	72	unsaturated	3:1 NH_4Cl, KCl fl.	CS20GL	0.057	0.022	RRO	2.19	6.41	18.82	0.013	0.006					M, Sp, Qtz, Cor, Qtz	
CS-NK-EXP56	CS $fO2$	775	0.20	48	unsaturated	3:1 NH_4Cl, KCl fl.	C3	0.049	0.013	IW	-5.09	6.41	18.82	0.204	0.014	0.031	0.011	0.192	0.056	M, Bio, K-spar, Na-spar, Cor, Qtz	
CS-NK-EXP58	CS $fO2$	750	0.20	24	unsaturated	3:1 NH_4Cl, KCl fl.	C3	0.044	0.017	IW	-5.16	6.41	18.82	0.147	0.017	0.048	0.023	0.196	0.045	M, Bio, K-spar, Na-spar, Cor, Qtz	
CS-NK-EXP59	CS time	775	0.20	24	unsaturated	3:1 NH_4Cl, KCl fl.	C3	0.058	0.018	NNO	0.00	6.41	18.82	0.066	0.010	0.026	0.022	0.059	0.023	M, Bio, K-spar, Na-spar, Cor, Qtz	
CS-NK-EXP60	P, CS time, CS $fO2$	775	0.20	96	unsaturated	NH_4Cl	HY3	0.019	0.019	NNO	-0.11	4.94	12.53	0.024	0.005			0.036	0.027	M, Bio, plag	
PC-NK-EXP3	PC $fO2$	750	0.95	30	unsaturated	3:1 NH_4Cl, KCl fl.	C2	0.003	0.030	WM	-5.01	6.41	18.82	0.563	0.029			0.554	0.057	M, Bio, Fa, Qtz	1
PC-NK-EXP4	PC $fO2$	750	0.95	46	unsaturated	3:1 NH_4Cl, KCl fl.	C2	0.004	0.030	WM	-5.01	6.41	18.82	1.119	0.137			0.808	0.043	M, Bio, Fa, Qtz	1
PC-NK-EXP9	P, PC time, PC $fO2$	775	0.95	40	unsaturated	NH_4Cl	HY3	0.010	0.010	NNO	-0.08	3.79	9.61	0.035	0.011			0.498	0.131	M, Bio, Pyx	
PC-NK-EXP10	PC time	775	0.95	25	unsaturated	NH_4Cl	HY3	0.011	0.011	NNO	-0.08	3.84	9.74	0.200	0.030			0.641	0.117	M, Bio, Pyx	
PC-NK-EXP11	PC time	810	0.95	1	unsaturated	NH_4Cl	HY3	0.007	0.007	NNO	-0.09	4.35	11.02	0.163	0.049					M, Pyx	
PC-NK-EXP12	P, PC time, PC $fO2$	800	0.95	50	unsaturated	NH_4Cl	HY3	0.008	0.008	NNO	-0.08	3.82	9.68	0.058	0.012			0.107	0.032	M, Bio, Pyx	
PC-NK-EXP13	PC time	800	0.95	5.5	unsaturated	NH_4Cl	HY3	0.009	0.009	NNO	-0.08	3.78	9.58	0.236	0.029			0.335	0.067	M, Bio, Pyx	
PC-NK-EXP14	P, PC time, PC $fO2$	800	0.95	95	unsaturated	NH_4Cl	HY3	0.006	0.006	NNO	-0.09	4.24	10.74	0.073	0.014			0.193	0.016	M, Bio, Pyx	
PC-NK-EXP17	P, Cl	800	1.62	63	unsaturated	NH_4Cl	HY3	0.006	0.006	NNO	-0.09	4.43	11.22	0.205	0.027			0.288	0.084	M, Bio, Pyx	
PC-NK-EXP18	P	800	2.28	47	unsaturated	NH_4Cl	HY3	0.006	0.006	NNO	-0.09	4.13	10.48	0.525	0.048			0.390	0.065	M, Bio, Amp, Qtz	
PC-NK-EXP19	T, P	800	1.90	54	unsaturated	NH_4Cl, KCl	HY3	0.008	0.008	NNO	-0.10	3.62	13.05	0.251	0.025			0.117	0.024	M, Bio, Amp, Qtz	
PC-NK-EXP21	T	875	1.90	45	unsaturated	NH_4Cl, KCl	HY3	0.006	0.006	NNO	-0.12	4.37	14.23	0.308	0.028			0.044	0.014	M, Bio, Pyx	
PC-NK-EXP22	T	925	1.90	46	unsaturated	NH_4Cl, KCl	HY3	0.006	0.006	NNO	-0.11	4.16	13.54	0.252	0.021			0.092	0.029	M, Bio, Pyx	
PC-NK-EXP23	T	775	1.90	91	unsaturated	NH_4Cl, KCl	HY3	0.006	0.006	NNO	-0.11	4.20	14.57			0.024	0.022	0.136	0.044	Bio, Amp, K-spar, Qtz	
PC-NK-EXP26	Cl	800	1.62	67	unsaturated	NH_4NO_3	HY3	0.007	0.008	NNO	-0.02	3.12	0.00	0.112	0.029			0.133	0.072	M, Bio, Amp	
PC-NK-EXP28	Cl	800	1.64	72	unsaturated	NH_4NO_3+NH_4Cl	HY3	0.008	0.010	NNO	-0.06	5.24	5.96	0.179	0.053			0.262	0.088	M, Bio, Pyx, Amp	
PC-NK-EXP31	Cl	800	1.70	74	unsaturated	NH_4NO_3+NH_4Cl	HY3	0.008	0.010	NNO	-0.05	5.65	2.72	0.177	0.040			0.13	0.06	M, Bio, Amp	

Note: Experiments with "3:1" and "1:1" fluid components contained the same composition fluid in the inner and outer capsule. Other experiments contained pure H_2O in the outer capsule. Columns labeled N fl. and Cl fl. refer to the initial inner capsule fluid. Phases: M = melt, Bio = biotite, Na-spar = Na-rich feldspar, K-spar = k-rich feldspar, Amp = amphibole, Pyx = pyroxene, Plag = plagiolcase, Fa = Fe-rich olivine, Cor = Al_2O_3, Qtz = SiO_2, Sp = spinel, 1 = PC_NK_EXP3+4 were cooled from 850 °C at 0.2/min, open inner cap

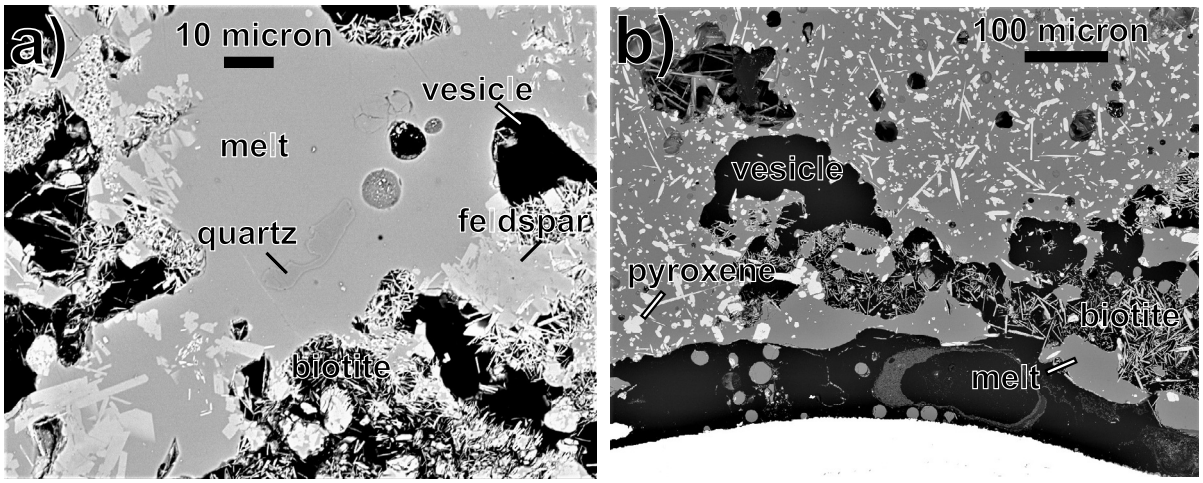

Fig. 2. Representative backscatter electron images of (a) CS series experiments (CS_NK_EXP34, P = 0.2 GPa, T = 725 °C, fO_2 = NNO+0) and (b) PC series experiments (PC_NK_EXP9, P = 0.95 GPa, T = 775 °C, fO_2 = NNO-0.08). CS series experiments (a) contain a quenched melt (dark), feldspar that grades from Na-rich core to K-rich rims, and relatively small laths of biotite. PC series experiments run with HY3 starting materials (b) contain a quenched melt, laths of biotite, and, in this example, pyroxene. Vesicles of varying size are present throughout all run products. Pt capsule is present in the bottom of the image.

when compared to the anhydrous high-silica standard glass DT-39 (a pantellerite) (Cottrell et al., 2009). This is consistent with longer Fe—O bonds and Fe in higher coordination in hydrous, quenched melt when compared to anhydrous melt (Wilke et al., 2006; Cottrell et al., 2018). Moreover, the melts quenched from the cold-seal apparatus have more structure near the main absorption edge and into the EXAFS energies compared to standard glasses, indicating shifts in Fe coordination due to the slower quench rates achievable in the cold-seal and the lower glass transition temperature of these hydrous high-silica compositions (Wilke et al., 2006). We could not determine the oxidation state of Fe in the glass because we lacked compositionally matched standards and because of the quench-modifications we describe above.

2.6. Experimental oxygen fugacity (fO_2)

We attempted to constrain experimental fO_2 using three methods: Fe-XANES on the quenched melt, the composition of the PtFe alloy of the capsule in contact with quenched melt, and the fO_2 corresponding to that of the solid fO_2 buffer employed in each experiment, taking the activity of water aH_2O (chemical activity of H_2O) into account.

As described above, Fe-XANES spectra revealed modification of Fe coordination upon quench, and could not be used to constrain fO_2.

The composition of the PtFe alloy did not correspond to fO_2 because, at the low temperatures of these experiments, PtFe intermetallic alloys formed with compositions insensitive to fO_2 (Supplementary Figure 6, Supplementary Table 6).

We therefore must assume that the experimental fO_2 is equivalent to that of the solid state buffer we employed, modified to account for the fact that aH_2O is not always equal between fluid in contact with the buffer and sample (Table 1). We employed a double capsule approach, where the fO_2 buffer was loaded into the outer capsule and the along with an inner, or sample, capsule. For the redox potential of the fO_2 buffer to be imposed directly on the sample capsule, aH_2O must be equivalent in the sample and the buffer. For experiments with "1:1" or "3:1" fluids, we achieved this by adding the same fluid to the outer and sample capsules. Here buffer fO_2 is assumed to equal the sample fO_2.

For experiments with HY3 starting silicate compositions, the sample capsule fluid and outer capsule fluid were not identical. Sample capsule fluids were generated by the decomposition of hydroxides and the addition of additional components, NH_4Cl, NH_4NO_3, and KCl, while the outer capsule fluid was pure H_2O. We calculate fO_2 for these experiments using the following expression:

$$\left(\quad fO_{2\ pure\ H_2O} \right) = 2\,log\,(aH_2O) \tag{4}$$

To calculate aH_2O we assume N was present as N_2, Cl was present as HCl, and that the mole fraction of H_2O equates to aH_2O. We don't account for the loss of H_2O from the fluid to the hydrous melt. If we assume melts in PC series experiments contained 30 wt.% H_2O, this could lead to up to a half log-unit reduction in fO_2 compared to our reported values. Assuming melt in CS series experiment contained 5 wt.% H_2O, would lead to at most a third of a log unit reduction in fO_2 compared to our calculations (Supplementary Information). Thus, any variations in fO_2 due to H_2O loss the will be systematic and should effect all experiments to similar degree. We verified fluid saturation for each experiment for both the outer and inner capsules after quench. We report the fO_2 of each experiment, relative to the NNO buffer, in Table 1 using data from O'Neill and Pownceby (1993) and Myers and Eugster (1983).

3. Results

3.1. Run products

All experiments contain a quenched rhyolitic melt that reacted with a hydrous fluid (~4 wt.% N and 0-15 wt.% Cl) at known fO_2, with the exception of PC_NK_EXP23 (no quenched melt identified). The presence of fluid was confirmed by the expulsion of fluid open piercing the inner capsule and large, circular void spaces in our run products (interpreted as vesicles). Starting silicate chemistry varied between CS series experiments leading to a range of mineral assemblages. CS series experiments with C, C1, C2, and HY3 composition silicate stabilized feldspar and biotite, while CS20GL starting composition experiments stabilized a Fe-Al spinel. Trace amounts of quartz and Al_2O_3 were observed in many CS series experiments (Fig. 2) that were only analyzed by energy dispersive spectroscopy for identification purposes. PC series experiments run with the C2 starting compositions contained biotite, fayalite, and quartz. PC series experiments that used HY3 stabilized biotite, pyroxene, and in some cases quartz and amphibole. Amphiboles were stabilized in higher pressure, lower temperature PC series experiments. We also note the presence of small diameter (<1-10 μm) spheres of silicate in regions that were occupied by fluid at high PT conditions

(Fig. 2b), and we interpret these features to reflect the exsolution of silicate from the hydrous fluid upon quench. The near-solidus PC series experiment (PC_NK_EXP23) additionally contained feldspar. Table 1 provides a listing of phases present in each experiment.

Fig. 2 provides representative backscatter electron images of CS and PC series experiments. CS experiments (Fig. 2a) contain large pools of quenched melt are commonly surrounded by feldspar that grades from Na-rich (dark) cores to K-rich (bright) edges. Biotite (backscatter bright) is found as small laths in the quenched melt, as is common observed (e.g., Vielzeuf and Montel, 1994). Abundant and larger biotite crystals (>10 μm), also grow in direct contact with hydrous fluid or near the melt-fluid interface. The size of bioite grains in contact with fluid tends to increase with pressure (cf., Fig. 2a, 2b, and Supplementary Figure 7).Vesicles (backscatter black) vary in size from <10 μm to >100 μm in diameter. PC series experiments run with HY3 starting materials (Fig. 2b) contain a quenched melt (backscatter dark), relatively larger laths of biotite than CS series experiments, vesicles (backscatter black), and other phases (pyroxene, amphibole, and quartz). Quenched melt in PC series experiments tends to be vesiculated on the micron-scale away from the rims. Chemical analyses from more and less vesiculated regions did not reveal obvious differences in N content. Biotite surfaces in all experiments are relatively rough; this is likely an artifact of sample preparation resulting from the small the small grain size, perfect cleavage, and low hardness. Rough surfaces may lead to additional analytical scatter on biotite (Table 1). Compositional analyses of biotite, quenched melt, K-rich feldspar, Na-rich feldspar, pyroxene, quartz, and amphibole are reported in Supplementary Tables 7-13, respectively. An additional backscatter electron image of PC_NK_EXP3 is provided in as Supplementary Figure 7.

3.2. Evaluation of equilibrium

3.2.1. Time series

A series of PC experiments were completed with durations ranging from 1 to 95 hours at NNO to constrain the time evolution of N partitioning in our experiments (Fig. 3a). Temperature within this series varied in a narrow window between 775 and 800 °C and pressure was fixed at 1 GPa.

Experiments run shorter than 30 hours consistently show higher $D^N_{melt-fluid}$ values. Experiments run longer than 30 hours yield similar and relatively low $D^N_{melt-fluid}$ values. We interpret this shift in behavior to reflect the time needed to oxidize and deprotonate the more melt soluble NH_4^+ species (the initial speciation of N) to N_2, NH_3, NH_2^-, or other less soluble species. Consequently, we only interpret PC experiments conducted for >30 hours at NNO as achieving equilibrium for the melt-fluid system.

A similar, but less distinctive, pattern is present within the time series run for CS experiments (Fig. 3b). Here the time to achieve a steady state distribution of N between melt and fluid is ∼70 hours. The time series for the CS experiments was conducted at lower temperatures compared to the PC series (725-775 versus 775-800 °C), which may explain the longer time to achieve equilibrium. The larger scatter in the CS series data likely reflects the overall lower concentration of N in the quenched melt of these experiments. For CS experiments at NNO, we conclude 70 hours is required to achieve melt-fluid equilibrium.

More reduced experiments (not plotted in Fig. 3) were run for shorter durations (24-48 hrs) to minimize and fluid loss from the experiment and the chance that the buffer would be exhausted due to the larger redox gradient between the capsule and pressure vessel. Direct evidence for more reduced experiments closely approaching melt-fluid equilibrium comes from their relatively small melt analysis standard deviations (% basis), the fact that the reduced quenched melts contain similar N concentrations despite

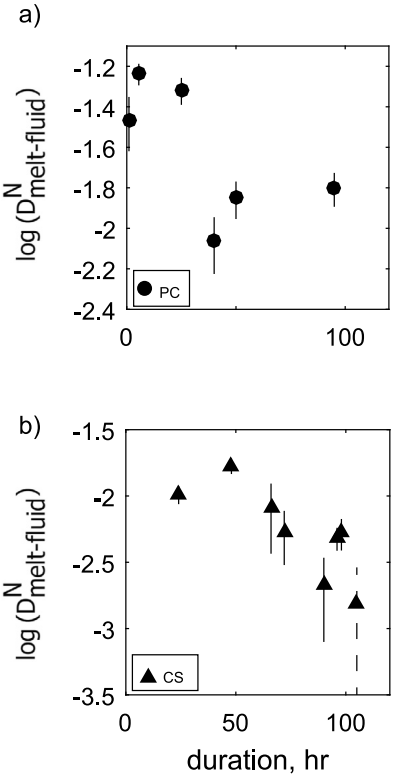

Fig. 3. Time series of melt-fluid partitioning results for (a) PC experiments and (b) CS experiments. In both series shorter duration experiments yield higher melt-fluid partitioning results. We interpret this to result from the gradual oxidization and deprotonation of NH_4^+. Dashed lines indicate error bars that extend off-scale.

being run over different durations (24-48 hrs), and the similar $log(D^N_{melt-fluid})$vs NNO slope determined in CS and PC series experiments (below).

3.2.2. Tests for homogenous nitrogen distribution in melts and minerals

We report simultaneous LDE1L and LDE5L analyses of N in quenched melt and biotite to evaluate N concentrations and heterogeneity within phases (Supplementary Figures 8-11 and Table 14). If individual N concentrations derived from simultaneous analysis with LDE5L and LDE1L crystals do not correlate, we assume that variability between the two measurements may be ascribed to analytical uncertainty. In contrast, if analyses obtained with LDE5L and LDE1L crystals correlate, we assume that variations reflect heterogeneity in the N concentration of that phase. A correlation (P-values <0.05) between LDE5L and LDE1L counts is only present in the biotite analyses of PC_NK_EXP9 and this phase is not included in partitioning comparisons for this experiment. Some individual measurements of biotite yield high concentrations of N and low concentration of K. These analyses likely indicate that some biotite grew early in our experiments before redox equilibrium was established and these biotite analysis are therefore discarded.

3.3. Oxygen fugacity controls on melt-fluid partitioning of nitrogen

Nitrogen speciation is predicted to vary under the range of *P-T-X* conditions associated with dehydrating and melting slabs (Mikhail and Sverjensky, 2014; Mikhail et al., 2017). More reduced conditions favor N-H species over N_2, while pH determines the relative stability of NH_3, NH_4^+, and NH_2^- (Reactions (1)-(3)). Prior experimental studies confirm these predictions, at least for the reduction of N_2 to N-H species (Mysen and Fogel, 2010; Li and Keppler, 2014; Li et al., 2015; Sokol et al., 2017; Mallik et al.,

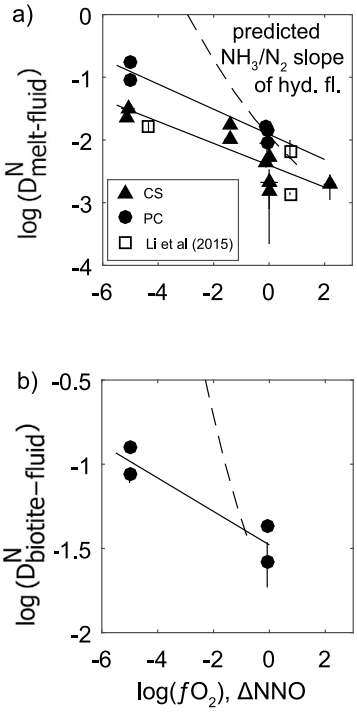

Fig. 4. Oxygen fugacity effect on a) melt-fluid and b) biotite-fluid partitioning of N. a) A melt-fluid redox series was conducted using both a cold seal (triangles) and piston cylinder (circles) apparatus. Slopes in a) are -0.20 ± 0.04 (R^2 = 0.94, P-value = 0.007) and -0.17 ± 0.04 (R^2 = 0.76, P-value = 0.002) for the PC and CS series, respectively. b) Our biotite-fluid fO_2 series yields a relatively shallow slope of -0.10 ± 0.04 (R^2 = 0.87, P-value = 0.07). The dashed lines are the predicted the fO_2 sensitivity of the within hydrous fluid from Li and Keppler (2014). We also plot for comparison in a) the melt-fluid partitioning data from Li et al. (2015), which were collected at similar *P-T-X* conditions as our cold series data (haplogranite, 0.2 GPa). Reducing conditions favor N incorporation in a) melt and b) biotite over fluid, but observed effects of redox (solid lines) on partitioning are moderate relative to the predicted fO_2 sensitivity of the hydrous fluid NH_3/N_2 ratio.

2018; Chen et al., 2019; Mosenfelder et al., 2019). Indeed, evidence for this in our own experiments comes from Raman spectra of a quenched melt from a reduced experiment (WM oxygen buffer, PC_NK_EXP3) that has a resolved, albeit muted, peak at ~3300 cm^{-1}, near the position associated with the most intense N-H band commonly observed in glasses (Mysen et al., 2008), while our more oxidized experiments (NNO oxygen buffer, PC_NK_EXP13 and 18) lack a defined peak in this same spectral region (Supplementary Figure 4, Supplementary Information). It is difficult, however, to determine the relative stability and reactivity of specific N-H species using spectroscopy of high *P-T* hydrous fluids (Schmidt and Watenphul, 2010). Thus, it is challenging to translate spectroscopic measurements into specific $D^N_{biotite-fluid}$ or $D^N_{melt-fluid}$ values, which control the behavior of N during slab dehydration and melting.

We report $D^N_{melt-fluid}$ and $D^N_{biotite-fluid}$ as a function of NNO to constrain the reactivity of N with melt and K-bearing minerals (Fig. 4). Separate melt-fluid fO_2 series were completed using a PC and CS apparatus, yielding log-log slopes of -0.20 ± 0.04 (R^2 = 0.94, P-value = 0.007) and -0.17 ± 0.04 (R^2 = 0.76, P-value = 0.002), respectively. Our biotite-fluid fO_2 series yields a relatively shallow slope of -0.10 ± 0.04 (R^2 = 0.87, P-value = 0.07).

Reaction (1) implies the following relationship between N speciation and fO_2:

$$fO_2^{-3/4} \propto aNH_4^+ / fN_2^{0.5} \quad (5)$$

or similarly

$$fO_2^{-3/4} \propto aNH_3 / fN_2^{0.5} \quad (6)$$

When N_2 dominates, aNH_4^+ and aNH_3 should decrease with increasing fO_2 according to -0.75 slope in log-log space at constant *P-T-pH* conditions. We plot, as dashed lines, the predicted fO_2 sensitivity of the NH_3/N_2 ratio calculated for a hydrous fluid with 5 mol% N at 775 °C and 1 GPa from Li and Keppler (2014). The relatively shallow partitioning slopes observed here compared to predicted NH_3/N_2 slopes are consistent with the majority of reduced N species being unreactive with silicate and remaining with the fluid (e.g., NH_3), while silicate-reactive species (e.g., NH_4^+) are minority constituents at pH values applicable to mica-bearing slab sections. A horizontal slope would indicate no silicate-reactive species are stabilized under reducing conditions. The shallower slope of the biotite-fluid fO_2 correlation compared to melt-fluid correlations may indicate that rhyolite melt incorporates some NH_3, NH_2^-, or NH_2^+ (Mysen et al., 2008; Mosenfelder et al., 2019), while biotite only accepts NH_4^+. Li et al. (2015) report $D^N_{melt-fluid}$ values over an equivalent range in fO_2 compared to the CS series also using a cold-seal apparatus that also suggest a shallow slope relating $D^N_{melt-fluid}$ to fO_2 in a Cl-free system. In combination, Fig. 4 highlights the likely variable speciation of N in minerals, melts, and fluids under slab-applicable *P-T-X* conditions. Fluid NH_3/N_2 ratios are not directly indicative of N reactivity with silicate.

3.4. Pressure effect on melt-fluid and mineral-melt partitioning of nitrogen

Pressure is predicted to affect $D^N_{melt-fluid}$ and $D^N_{biotite-fluid}$ in several ways. First, reduced N-H species (NH_4^+ and NH_3) are stabilized over N_2, and NH_4^+ is stabilized over NH_3 following the volume changes associated with each species formation (Schmidt and Watenphul, 2010; Mikhail and Sverjensky, 2014; Li and Keppler, 2014; Sokol et al., 2017). Second, neutral species solubility (e.g., NH_3 and N_2) increases in melt and minerals according to their respective Henry's Law constants. Evidence for this comes from quenched melt in our highest pressure experiment (PC_NK_EXP18) having a relatively strong N_2 Raman band compared to a lower pressure experiment in the pressure series (PC_NK_EXP13) (Supplementary Figure 4). Other experimental work has also linked increased pressure with higher $D^N_{melt-fluid}$ values (e.g., Mallik et al., 2018; Förster et al., 2019). To further quantify the effect of pressure on $D^N_{melt-fluid}$ and $D^N_{biotite-fluid}$ values, we completed a series of experiments between 0.2 and 2.3 GPa (Fig. 5). Temperature was varied in a narrow range between 775 and 800 °C. NNO buffers were used in all pressure-series experiments.

Regression of $\log(D^N_{melt-fluid})$ against P/T (GPa/K) yields a slope of 761 ± 68 (R^2 = 0.97, P-value <0.001) (Fig. 5a). We compare the pressure dependencies of $D^N_{melt-fluid}$ and NH_3/N_2 ratios of N-bearing fluids (dotted line, Li and Keppler (2014)). Both $D^N_{melt-fluid}$ and NH_3/N_2 ratios correlate with pressure, but the slope for $D^N_{melt-fluid}$ is ~2× greater than that predicted by the fluid NH_3/N_2 ratio. The strong dependence of $D^N_{melt-fluid}$ on pressure may indicate that pressure stabilizes NH_4^+ over NH_3, and/or that neutral species (NH_3 and N_2) concentration in melt increases with pressure. Indeed, evidence for the role of neutral species in determining melt solubility comes from the greater dependence of $\log(D^N_{melt-fluid})$ on P/T than $\log(D^N_{biotite-fluid})$ (Fig. 5b, 462 ± 169, R^2 = 0.71, P-value = 0.04), and the dependence of $\log(D^N_{biotite-melt})$ on P/T being negative (-273 ± 158, R^2 = 0.49, P-value=0.12), albeit less well defined.

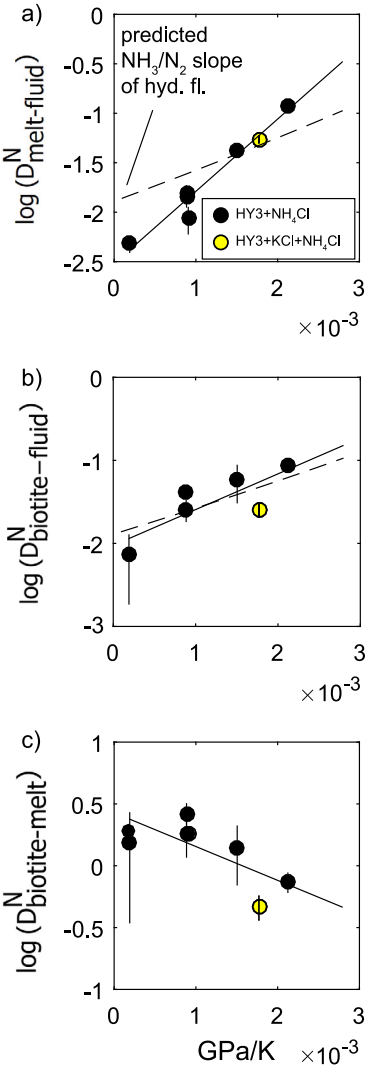

Fig. 5. Pressure effect on (a) melt-fluid, (b) biotite-fluid partitioning, and (c) biotite-melt partitioning. The role of pressure is to increase the partitioning of N into silicate (a and b), although the effect is larger for melt compared to biotite (c). Observed pressure effects on $\log(D^N_{melt-fluid})$ and $\log(D^N_{biotite-fluid})$ is less than and similar to, respectively, that predicted by Li and Keppler (2014) for NH_3/N_2 ratios of hydrous fluid (dashed lines in a and b). Data are recalculated to NNO using the PC series correlation in Fig. 4.

3.5. Temperature effect on melt-fluid and mica-fluid partitioning of nitrogen

Theory and experiment predict that higher temperatures favor N_2 over NH_4^+ and NH_3 and favor NH_3 over NH_4^+ (Schmidt and Watenphul, 2010; Mikhail and Sverjensky, 2014; Li and Keppler, 2014; Sokol et al., 2017; Chen et al., 2019). Both factors should lead to a positive correlation between inverse temperature (1000/K) and nitrogen partitioning between silicate phases and fluid (i.e. $D^N_{melt-fluid}$ and $D^N_{biotite-fluid}$). To test these predictions, we conducted a series of PC experiments between 775 and 925 °C (Fig. 6). Pressure was fixed at 2 GPa, and NNO oxygen buffers were used in all experiments. All temperature series data are recalculated to a common P/T value (2×10^{-3} GPa/K) to account for the pressure effect (Fig. 5). Note the experiment conducted at 775 °C did not contain sufficient melt for analysis.

Fig. 6 plots the temperature series for $D^N_{melt-fluid}$ and $D^N_{biotite-fluid}$ results. The $\log(D^N_{melt-fluid})$-1000/K slope is -854 ± 823 (R^2 = 0.78, P-value = 0.31). The $\log(D^N_{biotite-fluid})$-1000/K slope is also poorly

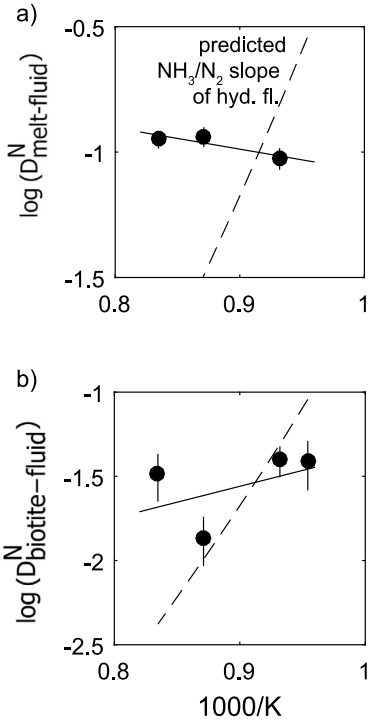

Fig. 6. Temperature effect on (a) melt-fluid and (b) biotite-fluid partitioning. Both series yield temperature effects that are within error of zero at the 95% confidence level. Predicted effects of temperature on NH_3/N_2 ratios of hydrous fluid from Li and Keppler (2014) on are plotted as dashed lines. The partitioning data show a weaker dependence on temperature compared NH_3/N_2 ratios of hydrous fluid. Data are recalculated to NNO and a common P/T value (2×10^{-3} GPa/K) using the correlations in Fig. 4 and 5.

defined at 1888 ± 3241 (R^2 = 0.23, P-value = 0.52). We do not resolve any statistically significant temperature effects on N partitioning.

The uncertainty associated with our N analyses precludes any definitive statement regarding the role of temperature in affecting silicate-fluid partitioning other than that it appears to be relatively minor compared to predicted NH_3/N_2 changes in fluid chemistry. This further emphasizes the fluid speciation cannot be used to directly infer N reactivity with silicate.

Other experimental determinations of temperature effects provide variable results. Förster et al. (2019) report that $D^N_{melt-fluid}$ values decrease with temperature, while Mallik et al. (2018) report no measurable effect of temperature on $D^N_{melt-fluid}$ at relatively high temperatures (1050-1300 °C, ~NNO-1).

3.6. Compositional effects on melt-fluid and mineral-fluid partitioning of nitrogen

Our experiments were designed to produce relatively large grains of K-bearing minerals in equilibrium with melt and hydrous fluid. The role of melt composition on N solubility was not investigated. All experimental melts were rhyolitic by design to be applicable to slabs during dehydration and melting (Johnson and Plank, 2000; Schmidt et al., 2004).

The exchange of NH_4^+ into K-sites in minerals may be affected by bulk mineral composition. To test for this effect, measured values of $D^N_{biotite-melt}$ and $D^N_{Kspar-melt}$ are plotted against mineralogical compositional parameters (Fig. 7a and b) (Mg# for biotite and Or# for feldspar, where (Mg# = Mg/(Fe+Mg) and Or# = Ab/(An+Or+Ab), molar bulk) and [N] of melt (Fig. 7c). The exchange of Mg for Fe in biotite does not strongly affect the partitioning of either $D^N_{biotite-melt}$ or $D^K_{biotite-melt}$ (Fig. 7a). We antic-

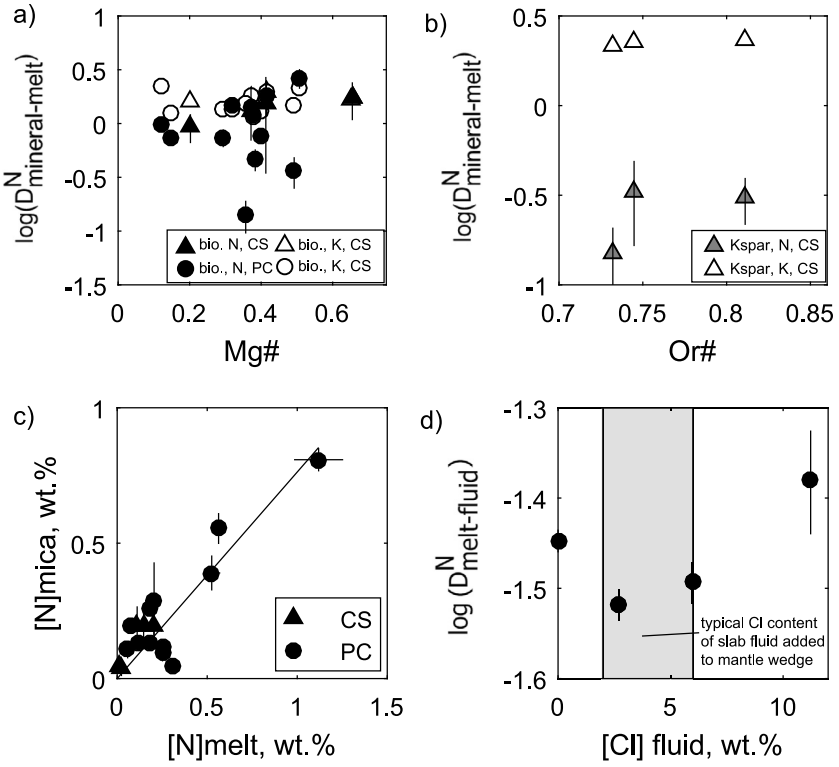

Fig. 7. The effect of compositional parameters (a) Mg#, (b) Or#, (c) [N]melt, and (d) [Cl] fluid on mineral-melt partitioning of N and K. (a and b) No obvious effects of compositional parameters are present. In general, K is more strongly partitioned into minerals compared to N and biotite has a greater affinity for N than feldspar. (c) Henrian partitioning behavior is observed between biotite and melt (R^2 = 0.90, P-value<0.001). d) Chlorine content of hydrous fluid is not strongly correlated with melt-fluid partitioning of N. Minor effects remain possible. The shaded region is the range of typical Cl content of slab fluid added to mantle wedge from Métrich and Wallace (2008).

ipated that $D^N_{Kspar-melt}$ would positively correlate with Or# given the ionic radius of NH_4^+ relative to K^+ and Na^+; however, Fig. 7b shows there is no measurable effect of K-Na exchange in feldspar on $D^N_{Kspar-melt}$ values. We suggest that a wider range in feldspar chemistry or greater analytical precision are needed is needed to document the likely correlation between Or# and $D^N_{Kspar-melt}$. This speculation is supported by the fact that no analyzed Na-rich feldspars contained N above background (Supplementary Table 10).

$D^N_{biotite-melt}$ values are consistently higher than $D^N_{Kspar-melt}$ (Fig. 7a and 7b). This is consistent with K-feldspar also more readily incorporating Na, indicating a smaller radius large-ion site relative to biotite, and with natural mineral pairs (Honma and Itihara, 1981). Muscovite and phengite also incorporate relatively large amounts of N (Pöter et al., 2004; Förster et al., 2019), and the combination of these results stresses the importance of mica, in its variety of forms, in modulating the N contents of slabs during dehydration and melting. Quartz, orthopyroxene, clinopyroxene, and amphibole were stable in a subset of PC series experiments (Table 1), and N analyses of these phases do not yield counts above background using the LDE1L diffracting crystal (Supplementary Tables 11-13). We conclude that these phases are not significant hosts for N in the presence of mica and stress that K-bearing minerals control the retention of N in slabs.

In Fig. 7c, we plot the concentration of N in melt against the concentration of N in biotite. N concentrations in the melt correlate with those in biotite (R^2 = 0.90, P-value <0.001). This is not a strict test of Henry's Law, as *P-T-*fO_2 conditions are not constant between data points. Nevertheless, it is clear that melt and biotite concentrations correlate. The K site occupancy by N within biotite approaches 30% in our experiments, near the limit of Henrian behavior identified for muscovite (Pöter et al., 2004).

We also quantify the effect of Cl on the partitioning of N between melt and hydrous fluid (Fig. 7d). This series of experiments varies the Cl content of the fluid between 0 and 11.2 wt.% Cl at NNO, ~1.7 GPa, and 800 °C. Chlorine is a major element in subduction zone settings. Indeed, Metrich and Wallace (2008) suggest the majority of fluids entering the mantle wedge contain between 2-6 wt.% Cl. Previous work on K partitioning in melt-fluid system demonstrates that Cl lowers $D^K_{melt-fluid}$ values, likely related to the stability of K-Cl species in the fluid (Reed et al., 2000). The lack of a strong correlation between $D^N_{melt-fluid}$ values and Cl content of fluids suggests that the effect of Cl on N solubility is nearly equal in melt and fluid, at least at the *P-T-X* conditions of the present experiments. The minor role of Cl in modulating N partitioning is consistent with the similarity of $D^N_{melt-fluid}$ values determined for the fO_2 series of this study (Cl-bearing) and Li et al. (2015) (Cl-free), plotted in Fig. 4.

4. Discussion

4.1. Application of nitrogen partitioning results to dehydrating slabs

We resolve two controls on N mobility during dehydration: fO_2 (Fig. 4) and the pressure-temperature ratio (P/T) (Fig. 5). Lower fO_2 and higher P/T conditions promote N partitioning into silicate (rhyolitic melt and K-bearing minerals) compared to fluid. The importance of fO_2 and P/T conditions in modulating N behavior in subduction zones has been suggested based on melt-fluid partitioning and speciation data (Mikhail et al., 2017; Mallik et al., 2018; Li and Keppler, 2014), but here we directly quantify the propensity for nitrogen to be retained in slabs through the application of mineral-fluid and mineral-melt data.

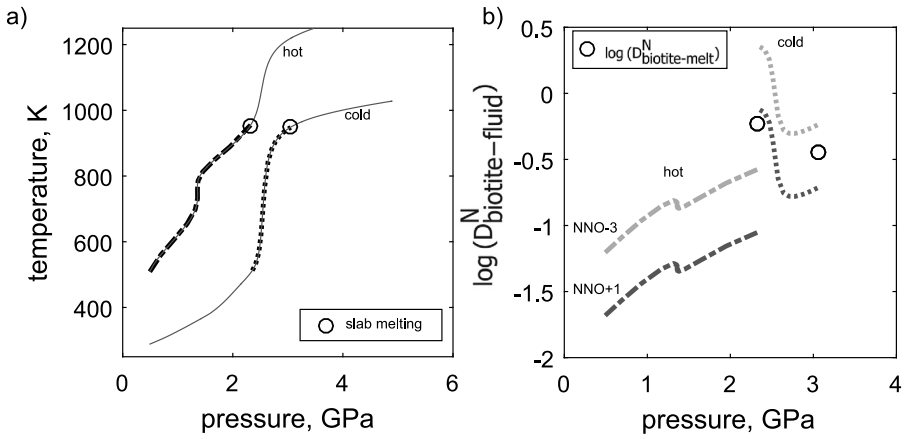

Fig. 8. (a) *PT* paths for hot and cold slabs. Dash and dash-dotted lines indicate the portion of the *PT* path where we calculate N partitioning in (b). Circles denote *PT* conditions for hot and cold slab melting calculations. (b) Predicted N partitioning behavior during dehydration along hot and cold *PT* paths with variable fO_2 conditions (shades of gray). Slab fO_2 ranges from reduced (light gray, NNO-3) to oxidized (dark gray, NNO+1) conditions. Hot and oxidizing conditions maximize N loss. Predicted $\log(D^N_{biotite-melt})$ values for slab melting of hot (left circle) and cold (right circle) slabs are similar to $\log(D^N_{biotite-fluid})$ values associated with dehydration under cold and reducing conditions.

A multiple linear regression on PC fO_2 and P/T series for mica-fluid data yields the following equation to predict N partitioning applicable to slab dehydration scenarios (R^2 = 0.75, P-value = 0.01):

$$log(D^N_{biotite-fluid}) = 429 \pm 135\frac{P}{T} - 0.12 \pm 0.04 \quad NNO - 1.98 \pm 0.18 \tag{7}$$

P is in GPa and T is in kelvin. We apply Eq. (7) to slabs dehydrating along hot (Cascadia) and cool (Honshu) geotherms with variable fO_2 (solid lines Fig. 8a). Geotherms are from Syracuse et al. (2010) from the D80 models for slab sediments. For hot slab scenarios, H_2O loss starts at 15 km depth (dash-dotted line, Fig. 8a), while for cold slab scenarios, H_2O loss starts at 80 km depth (dotted line, Fig. 8a). These conditions are derived from the petrological-thermal modeling of turbidite-bearing slabs where 1) in cold scenarios, dehydration mostly occurs as the slab first encounters the mantle wedge at 80 km depth, while 2) in hot scenarios, dehydration is a more continuous process from low to high pressure conditions (van Keken et al., 2011). Beyond 100 km, the P/T ratios of near-slab surface geotherms increase with depth, rapidly so for cooler slabs (Fig. 8a), limiting N extraction via dehydration deeper within subduction zones.

We range the fO_2 of slabs between NNO-3 to NNO+1 (Fig. 8b). This range is bracketed by the fO_2 of relatively oxidized primitive arc basalt (NNO+1, Cottrell et al., in press) and by lower range of fO_2 recorded by ecologite xenoliths at ~100 km depth (NNO-3) (Stagno et al., 2015).

An important caveat is that Eq. (7) is derived from experiments that contain a hydrous fluid with relatively high concentrations of N, ~4 wt.% (Table 1). The reduction of N_2 to N-H species with single N atoms (Reactions (1)-(3)) implies that the bulk concentration of N in the fluid will influence speciation. If Reactions (1)-(3) control speciation under natural conditions, higher [N] fluid will favor N_2 over NH_4^+, with lower corresponding silicate reactivity. Phengite is also likely the stable mica in Mg-FeO poor lithologies (Johnson and Plank, 2000; Schmidt et al., 2004), such as slab sediments, and recent results indicate $D^N_{phengite-melt}$ may be up to 3× lower than $D^N_{biotite-melt}$ values (Förster et al., 2019).

All dehydration scenarios predict that N behaves as an incompatible element during slab dehydration, except under the coolest and most reducing conditions considered here. We predict that hot slabs have relatively low associated $D^N_{biotite-fluid}$ values, only surpassing 0.1 under reducing (<NNO-2) conditions at pressure above 1 GPa. The mobility of N in hot slabs reflects their low P/T ratio dehydration conditions. Cold slabs are correspondingly retentive of N due to their higher P/T ratio dehydration conditions (Fig. 8b). Indeed, if dehydration occurs within a cold slab under reducing conditions (<NNO-2), we predict initial $D^N_{biotite-fluid}$ values greater than 1. Corroboration of the P/T effect on N mobility during dehydration comes from the observed massive N loss recorded in the hotter prograde sequences (Catlina Schist, Bebout and Fogel, 1992) compared to minimal N loss recorded in the cooler prograde sequences (Schistes Lustres nappe, Busigny et al., 2003).

Our mineral-fluid modeling quantifies the dual importance of slab fO_2 and subduction geotherm in determining the mobility of N during dehydration over geologically relevant conditions. An earlier Earth, with warmer slabs, and consequently lower P/T dehydration during subduction, would have been most prone to accumulating N within near-surface reservoirs (Fig. 8, Förster et al., 2019). With time, cooler slabs come to dominate and likely accelerate deep volatile cycles within Earth (Busigny et al., 2003; van Keken et al., 2011; Smye et al., 2017; Parai and Mukhopadhyay, 2018). Despite the current dominance of cool slabs, N remains partitioned into near-surface reservoirs relative to the other chemically reactive, volatile elements (Fig. 1a), and observational evidence is most consistent with p_{N2} increasing with time (Marty et al., 2013; Som et al., 2016). In this context, we suggest that oxidizing conditions, perhaps more so than what is observed within arc basalts (>NNO, Cottrell et al., in press), may be required within the uppermost slab sections to promote partitioning of N into near-surface reservoirs over C and H (Fig. 1a).

4.2. Application of nitrogen partitioning results to melting slabs

Nitrogen loss from slabs may also occur due to melting. In this case mineral-melt partitioning will dictate the rate at which N is extracted from the slab. Micas remain stable beyond the fluid-saturated solidus of sediments (~675 °C, e.g., Schmidt et al., 2004), and it is therefore expected that micas will also control the retention of N during slab melting. We plot in Fig. 8a the P/T values (circles) associated with the slab reaching 675 °C. The correlation in Fig. 5c provides the following relationship for $D^N_{biotite-melt}$ values:

$$log\ (D^N_{biotite-melt}) = -273 \pm 158\frac{P}{T} - 0.43 \pm 0.22 \tag{8}$$

In Fig. 8b we plot the associated predicted $D^N_{biotite-melt}$ values for hot and cold slab melting using Eq. (8) (circles). Absolute

$D^N_{biotite-melt}$ values are relatively high compared to $D^N_{biotite-fluid}$ predicted for hot and/or oxidized slabs. We conclude that melting is a relatively inefficient mechanism for N extraction on a mass loss from slab basis compared most dehydration scenarios.

4.3. Nitrogen-potassium coupling and the redox barrier to N subduction

As emphasized above, N-Ar systematics of MORB vesicles are well explained by mixing between a mantle reservoir with a nearly constant N/^{40}Ar ratio and different surficial reservoirs with lower N/^{40}Ar ratios (Fig. 1b). Because ^{40}Ar is the decay product of K, divergent behavior of N and K in their respective deep cycles should be manifested as variable N/^{40}Ar ratios in MORB mantle. Muted N/^{40}Ar variability in MORB mantle therefore implies a limited range of N/K ratios for materials recycled into MORB mantle (Marty, 1995; Johnson and Goldblatt, 2015), although rapid mixing of MORB mantle will also act to homogenize N/^{40}Ar and N/K heterogeneity with time. Nonetheless, Fig. 8 demonstrates that fO_2 and slab geotherms have potentially strong controls on the fraction of N retained in a subducted slab, and therefore its N/K ratio. If the prevailing fO_2 or slab geotherms have varied widely in time or between subduction zones, then this should result in variations of the N/K ratio of materials input back into the mantle. Yet, MORB yield a relatively limited range N/^{40}Ar, perhaps with minor differences between E-MORB and N-MORB (Fig. 1b, Marty and Dauphas, 2003, Marty and Zimmermann, 1999). Therefore, the relative constancy of the time-integrated N/K ratio implies a limited range of slab fO_2 and slab geotherms are recorded in melts derived from MORB mantle.

CRediT authorship contribution statement

All authors contributed to the drafting and revision of the manuscript. Jackson performed the experiments, prepared the experiments, completed the microprobe analysis, completed the Raman measurements, and completed the first draft of the manuscript. Cottrell contributed to the collection and interpretation of the XANES data. Andrews facilitated the cold seal experiments.

Declaration of competing interest

The authors declare no conflicts of interest.

Acknowledgements

We thank George Flowers, Anette von der Handt, Tim Rose, Sami Mikhail, Eleanor Mare, Tim Gooding, and Megan Holycross for discussions in support of this manuscript. We additionally thank Yuan Li, Ananya Mallik, and an anonymous reviewer for their constructive and thorough reviews. CRMJ acknowledges support by NSF-EAR grant 1725315, Smithsonian GVP fellowship, and startup from Tulane University. Portions of this work were performed at GeoSoilEnviroCARS (The University of Chicago, Sector 13), the Advanced Photon Source, Argonne National Laboratory. GeoSoilEnviroCARS is supported by the National Science Foundation—Earth Sciences (EAR-1128799) and the Department of Energy—GeoSciences (DE-FG02-94ER14466). This research used resources of the Advanced Photon Source, a US Department of Energy (DOE) Office of Science User Facility operated for the DOE Office of Science by Argonne National Laboratory under contract number DE-AC02-06CH11357. We thank Tony Lanzirotti and Matt Newville for their support at the beamline.

Appendix A. Supplementary material

Supplementary material related to this article can be found online at https://doi.org/10.1016/j.epsl.2020.116615.

References

Bebout, G.E., Fogel, M.L., 1992. Nitrogen isotope compositions of metasedimentary rocks in the Catalina Schist – implications for metamorphic devolatilization history. Geochim. Cosmochim. Acta 56 (7), 2839–2849.
Beran, A., Armstrong, J., Rossman, G.R., 1992. Infrared and electron microprobe analysis of ammonium ions in hyalophane feldspar. Eur. J. Mineral. 4 (4), 847–850.
Busigny, V., Cartigny, P., Philippot, P., Ader, M., Javoy, M., 2003. Massive recycling of nitrogen and other fluid-mobile elements (K, Rb, Cs, H) in a cold slab environment: evidence from HP to UHP oceanic metasediments of the Schistes Lustres nappe (western Alps, Europe). Earth Planet. Sci. Lett. 215 (1–2), 27–42.
Busigny, V., Cartigny, P., Laverne, C., Teagle, D., Bonifacie, M., Agrinier, P., 2019. A reassessment of the nitrogen geochemical behavior in upper oceanic crust from Hole 504B: implications for subduction budget in Central America. Earth Planet. Sci. Lett. 525, 115735.
Cannaò, E., Tiepolo, M., Bebout, G., Scambelluri, M., 2020. Into the deep and beyond: carbon and nitrogen subduction recycling in secondary peridotites. Earth Planet. Sci. Lett. 543, 116328.
Chen, Q., Zhang, Z., Wang, Z., Li, W.-C., Gao, X.-Y., Ni, H., 2019. In situ Raman spectroscopic study of nitrogen speciation in aqueous fluids under pressure. Chem. Geol. 506, 51–57.
Cottrell, E., Kelley, K.A., Lanzirotti, A., Fischer, R.A., 2009. High-precision determination of iron oxidation state in silicate glasses using XANES. Chem. Geol. 268 (3), 167–179.
Cottrell, E., Lanzirotti, A., Mysen, B., Birner, S., Kelley, K.A., Botcharnikov, R., Davis, F.A., Newville, M., 2018. A Mössbauer-based XANES calibration for hydrous basalt glasses reveals radiation-induced oxidation of Fe. Am. Mineral., J. Earth Planet. Mater 103 (4), 489–501.
Cottrell, E., Birner, S., Brounce, M., Davis, F.A., Waters, L.E., Kelley, K.A., in press. Oxygen fugacity across tectonic settings. In: Neuville, D.R., Moretti, R. (Eds.), AGU Geophysical Monograph, Redox Variables and Mechanisms in Magmatism and Volcanism. Wiley. https://doi.org/10.1002/essoar.10502445.1.
Förster, M.W., Foley, S.F., Alard, O., Buhre, S., 2019. Partitioning of nitrogen during melting and recycling in subduction zones and the evolution of atmospheric nitrogen. Chem. Geol. 525, 334–342.
Halama, R., Bebout, G.E., John, T., Scambelluri, M., 2014. Nitrogen recycling in subducted mantle rocks and implications for the global nitrogen cycle. Int. J. Earth Sci. 103 (7), 2081–2099.
Halama, R., Bebout, G.E., Marschall, H.R., John, T., 2016. Fluid-induced breakdown of white mica controls nitrogen transfer during fluid-rock interaction in subduction zones. Int. Geol. Rev.
Halliday, A.N., 2013. The origins of volatiles in the terrestrial planets. Geochim. Cosmochim. Acta 105, 146–171.
Honma, H., Itihara, Y., 1981. Distribution of ammonium in minerals of metamorphic and granitic-rocks. Geochim. Cosmochim. Acta 45 (6), 983–988.
Jackson, C.R.M., Parman, S.W., Kelley, S.P., Cooper, R.F., 2015. Light noble gas dissolution into ring structure-bearing materials and lattice influences on noble gas recycling. Geochim. Cosmochim. Acta 159 (0), 1–15.
Johnson, B., Goldblatt, C., 2015. The nitrogen budget of Earth. Earth-Sci. Rev. 148, 150–173.
Johnson, M.C., Plank, T., 2000. Dehydration and melting experiments constrain the fate of subducted sediments. Geochem. Geophys. Geosyst. 1 (12).
Krantz, J.A., Parman, S.W., Kelley, S.P., 2019. Recycling of heavy noble gases by subduction of serpentinite. Earth Planet. Sci. Lett. 521, 120–127.
Li, L., Bebout, G.E., Idleman, B.D., 2007. Nitrogen concentration and delta N-15 of altered oceanic crust obtained on ODP Legs 129 and 185: insights into alteration-related nitrogen enrichment and the nitrogen subduction budget. Geochim. Cosmochim. Acta 71 (9), 2344–2360.
Li, Y., Keppler, H., 2014. Nitrogen speciation in mantle and crustal fluids. Geochim. Cosmochim. Acta 129, 13–32.
Li, Y., Huang, R., Wiedenbeck, M., Keppler, H., 2015. Nitrogen distribution between aqueous fluids and silicate melts. Earth Planet. Sci. Lett. 411, 218–228.
Libourel, G., Marty, B., Humbert, F., 2003. Nitrogen solubility in basaltic melt. Part I. Effect of oxygen fugacity. Geochim. Cosmochim. Acta 67 (21), 4123–4135.
Mallik, A., Li, Y., Wiedenbeck, M., 2018. Nitrogen evolution within the Earth's atmosphere–mantle system assessed by recycling in subduction zones. Earth Planet. Sci. Lett. 482, 556–566.
Marty, B., 1995. Nitrogen-content of the mantle inferred from N_2-Ar correlation in Oceanic Basalts. Nature 377 (6547), 326–329.
Marty, B., 2012. The origins and concentrations of water, carbon, nitrogen and noble gases on Earth. Earth Planet. Sci. Lett. 313, 56–66.
Marty, B., Dauphas, N., 2003. The nitrogen record of crust-mantle interaction and mantle convection from Archean to present. Earth Planet. Sci. Lett. 206 (3–4), 397–410.
Marty, B., Zimmermann, L., 1999. Volatiles (He, C, N, Ar) in mid-ocean ridge basalts: assesment of shallow-level fractionation and characterization of source composition. Geochim. Cosmochim. Acta 63 (21), 3619–3633.
Marty, B., Zimmermann, L., Pujol, M., Burgess, R., Philippot, P., 2013. Nitrogen isotopic composition and density of the Archean atmosphere. Science 342 (6154), 101–104.

Métrich, N., Wallace, P.J., 2008. Volatile abundances in basaltic magmas and their degassing paths tracked by melt inclusions. Rev. Mineral. Geochem. 69 (1), 363–402.
Mikhail, S., Sverjensky, D.A., 2014. Nitrogen speciation in upper mantle fluids and the origin of Earth's nitrogen-rich atmosphere. Nat. Geosci. 7 (11), 816–819.
Mikhail, S., Barry, P.H., Sverjensky, D.A., 2017. The relationship between mantle pH and the deep nitrogen cycle. Geochim. Cosmochim. Acta 209, 149–160.
Mingram, B., Bräuer, K., 2001. Ammonium concentration and nitrogen isotope composition in metasedimentary rocks from different tectonometamorphic units of the European Variscan Belt. Geochim. Cosmochim. Acta 65 (2), 273–287.
Mosenfelder, J.L., Von Der Handt, A., Füri, E., Dalou, C., Hervig, R.L., Rossman, G.R., Hirschmann, M.M., 2019. Nitrogen incorporation in silicates and metals: results from SIMS, EPMA, FTIR, and laser-extraction mass spectrometry. Am. Mineral., J. Earth Planet. Mater. 104 (1), 31–46.
Myers, J.t., Eugster, H., 1983. The system Fe-Si-O: Oxygen buffer calibrations to 1,500 K. Contrib. Mineral. Petrol. 82 (1), 75–90.
Mysen, B.O., Fogel, M.L., 2010. Nitrogen and hydrogen isotope compositions and solubility in silicate melts in equilibrium with reduced (N plus H)-bearing fluids at high pressure and temperature: effects of melt structure. Am. Mineral. 95 (7), 987–999.
Mysen, B.O., Yamashita, S., Chertkova, N., 2008. Solubility and solution mechanisms of NOH volatiles in silicate melts at high pressure and temperature-amine groups and hydrogen fugacity. Am. Mineral. 93 (11–12), 1760–1770.
O'Neill, H.S.C., Pownceby, M.I., 1993. Thermodynamic data from redox reactions at high temperatures. I. An experimental and theoretical assessment of the electrochemical method using stabilized zirconia electrolytes, with revised values for the Fe-"FeO", Co-CoO, Ni-NiO and Cu-Cu_2O oxygen buffers, and new data for the W-WO_2 buffer. Contrib. Mineral. Petrol. 114 (3), 296–314.
Palya, A.P., Buick, I.S., Bebout, G.E., 2011. Storage and mobility of nitrogen in the continental crust: evidence from partially melted metasedimentary rocks, Mt. Stafford, Australia. Chem. Geol. 281 (3–4), 211–226.
Parai, R., Mukhopadhyay, S., 2018. Xenon isotopic constraints on the history of volatile recycling into the mantle. Nature 560 (7717), 223.
Plessen, B., Harlov, D.E., Henry, D., Guidotti, C.V., 2010. Ammonium loss and nitrogen isotopic fractionation in biotite as a function of metamorphic grade in metapelites from western Maine, USA. Geochim. Cosmochim. Acta 74 (16), 4759–4771.
Pöter, B., Gottschalk, M., Heinrich, W., 2004. Experimental determination of the ammonium partitioning among muscovite, K-feldspar, and aqueous chloride solutions. Lithos 74 (1–2), 67–90.
Reed, M.J., Candela, P.A., Piccoli, P.M., 2000. The distribution of rare Earth elements between monzogranitic melt and the aqueous volatile phase in experimental investigations at 800 C and 200 MPa. Contrib. Mineral. Petrol. 140 (2), 251–262.
Sadofsky, S.J., Bebout, G.E., 2000. Ammonium partitioning and nitrogen-isotope fractionation among coexisting micas during high-temperature fluid-rock interactions: examples from the New England Appalachians. Geochim. Cosmochim. Acta 64 (16), 2835–2849.
Schmidt, M.W., Vielzeuf, D., Auzanneau, E., 2004. Melting and dissolution of subducting crust at high pressures: the key role of white mica. Earth Planet. Sci. Lett. 228 (1–2), 65–84.
Schmidt, C., Watenphul, A., 2010. Ammonium in aqueous fluids to 600 degrees C, 1.3 GPa: a spectroscopic study on the effects on fluid properties, silica solubility, and K-feldspar to muscovite reactions. Geochim. Cosmochim. Acta 74 (23), 6852–6866.
Smye, A.J., Jackson, C.R., Konrad-Schmolke, M., Hesse, M.A., Parman, S.W., Shuster, D.L., Ballentine, C.J., 2017. Noble gases recycled into the mantle through cold subduction zones. Earth Planet. Sci. Lett. 471, 65–73.
Sokol, A.G., Palyanov, Y.N., Tomilenko, A.A., Bul'bak, T.A., Palyanova, G.A., 2017. Carbon and nitrogen speciation in nitrogen-rich C–O–H–N fluids at 5.5–7.8 GPa. Earth Planet. Sci. Lett. 460, 234–243.
Som, S.M., Buick, R., Hagadorn, J.W., Blake, T.S., Perreault, J.M., Harnmeijer, J.P., Catling, D.C., 2016. Earth's air pressure 2.7 billion years ago constrained to less than half of modern levels. Nat. Geosci.
Stagno, V., Frost, D.J., McCammon, C.A., Mohseni, H., Fei, Y., 2015. The oxygen fugacity at which graphite or diamond forms from carbonate-bearing melts in eclogitic rocks. Contrib. Mineral. Petrol. 169 (2), 16.
Syracuse, E.M., van Keken, P.E., Abers, G.A., 2010. The global range of subduction zone thermal models. Phys. Earth Planet. Inter. 183 (1–2), 73–90.
van Keken, P.E., Hacker, B.R., Syracuse, E.M., Abers, G.A., 2011. Subduction factory: 4. Depth-dependent flux of H(2)O from subducting slabs worldwide. J. Geophys. Res., Solid Earth 116.
Vielzeuf, D., Montel, J.M., 1994. Partial melting of metagreywackes. Part I. Fluid-absent experiments and phase relationships. Contrib. Mineral. Petrol. 117 (4), 375–393.
Wilke, M., Schmidt, C., Farges, F., Malavergne, V., Gautron, L., Simionovici, A., Hahn, M., Petit, P.-E., 2006. Structural environment of iron in hydrous aluminosilicate glass and melt-evidence from X-ray absorption spectroscopy. Chem. Geol. 229 (1–3), 144–161.